Gravitational wave beacons

Carlos O. Lousto and James Healy
Center for Computational Relativity and Gravitation, School of Mathematical Sciences, Rochester Institute of Technology, 85 Lomb Memorial Drive, Rochester, New York 14623, USA

(Received 18 May 2018; revised manuscript received 19 November 2018; published 18 March 2019)

We explore spinning, precessing, unequal mass binary black holes to display the long-term orbital angular momentum, $\vec{L}$, flip dynamics. We study two prototypical cases of binaries with mass ratios $q = 1/7$ and $q = 1/15$ and a misaligned spin of the large black hole (with an intrinsic spin magnitude of $S_2/m_2^2 = 0.85$). We conduct full numerical simulations, for nearly 14 and 18 orbits, respectively, to evolve the binary down to a merger and display a full L-flip cycle. The pattern of radiation of such systems is particularly interesting, displaying strong polarization-dependent variation of amplitudes at precessional frequencies, leading to distinctive observational consequences for gravitational wave detectors. These waveform features are strongly directional dependent, and measurements of gravitational wave polarizations can be exploited to disentangle the binary's parameters in various astrophysical scenarios.

DOI: 10.1103/PhysRevD.99.064023

I. INTRODUCTION

The late orbital dynamics of spinning binary black holes remains a fascinating area of research, especially since the numerical breakthroughs [1–3] solved the binary black hole problem, making it possible to study these systems via supercomputer simulations. The understanding of the role individual spins play during the late binary dynamics is particularly interesting, since it provides the means to extract these astrophysically crucial parameters from current and future gravitational wave observations.

Among the notable spin effects (without Newtonian analogs) observed in supercomputer simulations are the hang-up effect [4,5], which prompts or delays the merger of binary black holes depending on the sign of the spin-orbit coupling $\vec{S} \cdot \vec{L}$, the large recoils of the final black hole remnant [6], reaching up to 5000 km/s [7]; the flip flop of black hole spins in a binary, passing from aligned to antialigned periods with respect to the orbital angular momentum [8]; and the alignment instability [9] (a case of imaginary flip-flop frequencies [10]).

In this paper, we discuss a two-case study of spinning binaries that lead to a total flip of the orbital angular momentum. These *beaconing* cases, unlike the flip flop of spins mentioned above coupling spin spin, may arise during the transitional precession between the two single precession stages (the initial $\vec{L}$-dominated and the final $\vec{S}$-dominated dynamics [11]) but applies to a much larger region of a binary's parameter space including antialigned spins. For small mass ratio binary systems ($q = m_1/m_2 < 1/4$) in retrograde orbits (not necessarily exactly antialigned), the beaconing stage occurs at a relatively common rate before the merger.

We are interested in studying the case where this transition occurs in the strong dynamical period of a late inspiral and merger (as opposed to the previously studied case of a low post-Newtonian order regime [11]) and display its potential observational consequences for different gravitational wave detectors. For instance, the observation of orbiting stellar mass binary black holes by LISA [12] can not only inform Earth-based observatories of this binary entering in the band [13], but also, in turn, by determining the precession parameters near the merger, will lead to strong constraints on the precursor binary observed in the LISA band.

II. NUMERICAL TECHNIQUES

We evolve the binary black hole datasets using the LazEv [14] implementation of the moving puncture approach [2] with the conformal function $W = \sqrt{\chi} = \exp(-2\phi)$ suggested by Ref. [15]. For the run presented here, we use centered, sixth-order finite differencing in space [16], a fourth-order Runge Kutta time integrator, and a seventh-order Kreiss-Oliger dissipation operator. Our code uses the EinsteinToolkit [17,18] Cactus [19] Carpet [20] infrastructure. The Carpet mesh refinement driver provides a "moving boxes" style of mesh refinement. In this approach, refined grids of fixed size are arranged about the coordinate centers of both holes. The evolution code then moves these fine grids about the computational domain by following the trajectories of the two black holes. We use AHFinderDirect [21] to locate apparent horizons. We measure the magnitude of the horizon spin using the *isolated horizon* algorithm detailed in Ref. [22] and as implemented in Ref. [23].

In the tables below, we measure radiated energy and linear and angular momentum, in terms of the radiative Weyl scalar ψ_4, using the formulas provided in Refs. [24,25]. We extract the radiated energy momentum at finite radius and extrapolate to $r = \infty$ with the perturbative extrapolation described in Ref. [26]. Quasicircular (low eccentricity) initial orbital parameters are computed using the post-Newtonian techniques described in Ref. [27]. A varying $\eta(W)$ gauge parameter [28] has been used for the $q = 1/15$ evolutions.

Numerous convergence studies of our simulations have been performed. In Appendix A of Ref. [29], we performed a detailed error analysis of a prototypical configuration with equal mass and spins aligned or antialigned with respect to the orbital angular momentum. We varied the initial separation of the binary, the resolutions, grid structure, waveform extraction radii, and the number of ℓ modes used in the construction of the radiative quantities. In Appendix B of Ref. [30], we calculated the finite observer location errors and performed convergence studies (with three different resolutions) for typical runs with mass ratio $(q = 1, 3/4, 1/2, 1/3)$. Further convergence studies reaching down to $q = 1/10$ for nonspinning binaries are reported in Ref. [31]. For very highly spinning black holes $(s/m^2 = 0.99)$, the convergence of evolutions was studied in Ref. [32] and for $(s/m^2 = 0.95)$ in Ref. [33]. A cross verification (including convergence of higher modes) with the totally independent SpEC code has been performed in Refs. [34,35] for GW150914 and GW170104 targeted simulations. A catalog of 320 Rochester Institute of Technology (RIT) simulations [36,37] can be found in Ref. [38], but the region of parameter space here discussed has not been previously studied with extensive convergence tests. For our current simulations, we monitor accuracy by measuring the conservation of the individual horizon masses and spins during evolution, as well as the level of satisfaction of the Hamiltonian and momentum constraints, to ensure reaching an accuracy consistent with our main conclusions (see Fig. 6).

III. RESULTS

In order to explore the L-flip precession regime during the late inspiral and merger phase, we study two binary systems bearing mass ratios of $q = 1/7$ and $q = 1/15$, respectively. Note that, in a previous study [39,40], we estimated the need of $q < 1/4$ in order for the transitional precession to occur before the merger. The chosen initial configurations are depicted in Fig. 1 and given in more detail in Table I, under the labels GWB7 and GWB15, respectively. Two other reference set of runs with the same mass ratios but with nonprecessing and nonspinning black holes are also reported here under the labels AS7, AS15, NS7, and NS15.

For the sake of the simplicity of the analysis and its relatively small influence on binaries of the chosen small mass ratios, we take the small hole to be spinless. We give a relatively large spin magnitude (0.85) to the larger black hole in a configuration that initially corresponds to a polar orbit of the small hole around the total angular momentum $\vec{J}$; i.e., initially $\vec{L}$ and $\vec{J}$ are perpendicular to each other.

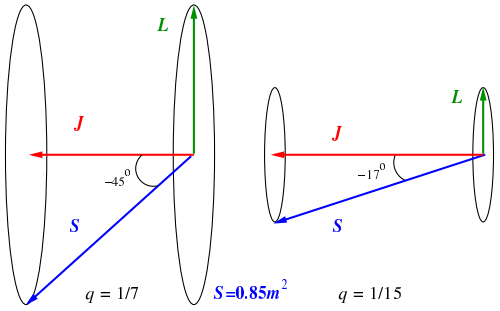

FIG. 1. Initial configuration of the orbital angular momentum $\vec{L}$, large hole spin $\vec{S}$, and total momentum of the system, $\vec{J}$. Both the spin and the orbital angular momentum precess (counterclockwise) around $\vec{J}$ as the system evolves.

The subsequent evolution of the two configurations leads to 14.5 orbits before the merger arises for the $q = 1/7$ case and 18 orbits before the merger arises for the $q = 1/15$ case. The direction of the total momentum $\vec{J}$ shows a notable stability during the whole simulations as displayed in Fig. 2, while its magnitude *grows* slightly due to a tendency towards alignment of the total spin, roughly as $J\dot{J} = -L\dot{L} > 0$. We also observe that the spin of the large hole, $\vec{S}_2$, and the orbital angular momentum $\vec{L}$ both precess counterclockwise around this almost constant total momentum direction $\hat{J} = \vec{J}/J$. During the simulation down to the merger, $\vec{L}$ completes 5/4 of a precession cycle (L flip) around $\vec{J}$ for the $q = 1/15$ case and 3/4 of a precession cycle around $\vec{J}$ for the $q = 1/7$ case.

In order to qualitatively understand the basic dependence of the beaconing phenomena on the binary parameters, we use a low order post-Newtonian analysis [see Eq. (3.2c) of Ref. [42]] with $\vec{S}_2 \cdot \hat{L} = -\vec{L} \cdot \hat{L}$ initially, to find a frequency of precession of $\vec{L}$:

$$M\Omega_L = 2\alpha_2^J/(1+q)^2(M/r)^3, \tag{1}$$

where r is the coordinate separation of the holes, $\alpha_2^J = \vec{S}_2 \cdot \hat{J}/m_2^2$ the dimensionless spin of the large hole along $\vec{J}$ (perpendicular to $\vec{L}$), $M = m_1 + m_2$ the total mass of the system, and $q = m_1/m_2 \leq 1$ its mass ratio.

The critical separation radius r_c, characterizing the middle of the transitional precession, where the condition $S_2^L = \vec{S}_2 \cdot \hat{L} = -\vec{L} \cdot \hat{L} = -L$ is met (for this condition to exist, r_c needs to be above the inclined isco radius [43]), is hence

TABLE I. Initial data parameters for the quasicircular configurations with a smaller mass black hole (labeled as 1) and a larger mass spinning black hole (labeled as 2). The punctures are located at $\vec{r}_1 = (x_1, 0, 0)$ and $\vec{r}_2 = (x_2, 0, 0)$ and have an initial simple proper distance [41] of d, with momenta $P = \pm(P_r, P_t, 0)$, mass parameters m^p/M, horizon (Christodoulou) masses m^H/M, total ADM mass $M_{\rm ADM}$, the dimensionless spin of the larger black hole $a_{2i}/m_2^H = S_i/m_H^2$ (with $a_{2y}/m_2^H = 0$ and $a_1^H/m_1^H = 0$), and the initial eccentricity e_0. The beaconing (nonprecessing, nonspinning) configurations are denoted by GWBX (ASX, NSX), where X gives the inverse mass ratio m_2^H/m_1^H.

Run	x_1/M	x_2/M	d/M	P_r/M	P_t/M	m_1^p/M	m_2^p/M	m_1^H/M	m_2^H/M	a_{2x}/m_2^H	a_{2z}/m_2^H	$M_{\rm ADM}/M$	e_0
GWB7	−11.594	1.656	16.6	$-8.724e-5$	0.036 01	0.119 940	0.459 292	0.1250	0.8750	−0.5993	−0.6028	0.996 57	0.0018
GWB15	−9.375	0.625	12.9	$-6.034e-5$	0.023 01	0.058 896	0.492 946	0.0625	0.9375	−0.8105	−0.2561	0.997 66	0.0071
AS7	−11.594	1.656	16.0	$-8.866e-5$	0.036 09	0.119 934	0.720 094	0.1250	0.8750	0.0000	−0.6028	0.996 57	0.0006
AS15	−9.375	0.625	11.9	$-6.443e-5$	0.023 23	0.058 879	0.908 436	0.0625	0.9375	0.0000	−0.2561	0.997 70	0.0011
NS7	−9.625	1.375	13.1	$-1.425e-4$	0.039 64	0.118 980	0.869 837	0.1250	0.8750	0.0000	0.0000	0.995 89	0.0006
NS15	−9.375	0.625	11.9	$-5.773e-5$	0.022 74	0.058 913	0.934 496	0.0625	0.8750	0.0000	0.0000	0.997 64	0.0006

$$(r_c/M)^{1/2} = (\alpha_2^L/2q)\left(1 + \sqrt{1 - 8(q/\alpha_2^L)^2}\right). \quad (2)$$

For the initial separation of the $q = 1/7$ simulation at ($r_c \approx 13M$), Eq. (1) leads to a period of $15\,042M$, while directly from the numerical waveform displayed in Fig. 3 we obtain $3025M$, counting from $t = 0$ to the first flip. So the estimated full beaconing period would at least be $4 * 3025 = 12\,100M$.

A basic comparison of those values with the orbital frequency in a post-Newtonian (PN) expansion [44]

$$M\Omega_{\rm orb} \approx \left(\frac{M}{r}\right)^{3/2} - \frac{3+5q+3q^2}{2(1+q)^2}\left(\frac{M}{r}\right)^{5/2} - \frac{2\alpha_2^L(1+4q) + q\alpha_1^L(3+2q+5q^2)}{2(1+q)^3}\left(\frac{M}{r}\right)^3 \quad (3)$$

leads to a period of $326M$, at this initial configuration.

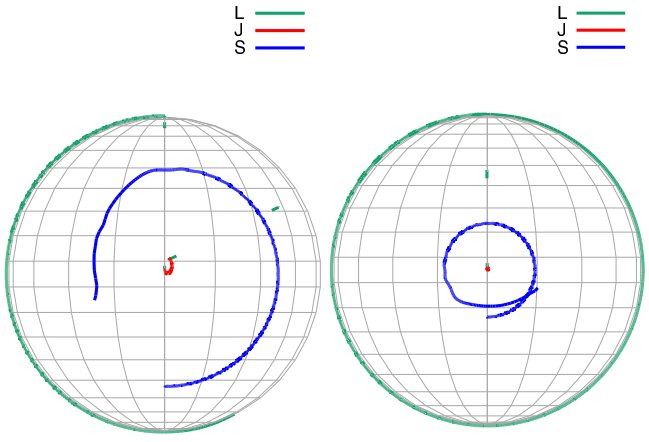

FIG. 2. Evolution of the directions of the orbital angular momentum $\vec{L}$, large hole spin $\vec{S}$, and total momentum of the system, $\vec{J}$. The spin and the orbital angular momentum precess (counterclockwise) around $\vec{J}$. As the system evolves, the loss of $\vec{L}$ does not seem to notably change the direction of $\vec{J}$ (see Table II below). Displayed on the left are the $q = 1/7$ and on the right the $q = 1/15$ binaries.

In the case of the simulation with mass ratio $q = 1/15$ (at initial $r_c \approx 10M$), guided by the waveform given in Fig. 4, we observe that from $t = 0$ to peak 1 in the beaconing amplitude we get $\approx 1111M$, from peak 1 of the phase to zero crossing $\approx 948M$, from zero crossing to peak $2 \approx 280M$, and from peak 2 to the merger $\approx 87M$. Using the initial first value, we find a period of modulation of $\approx 4444M$, which is in good agreement with the period derived from Eq. (1) of $4410M$. Similarly, the initial orbital period from Eq. (3) is $230M$.

The complete flip of the orbital angular momentum has dramatic effects on the pattern of gravitational radiation as seen by observers far from the binary system. At directions near perpendicular to the total angular momentum $\vec{J}$, radiation passes from periods of full amplitude, when the system is face on to periods of strong suppression when the system is face off. This *beaconing* phenomenon is displayed in Fig. 5 for the $q = 1/15$ case and may have important observational consequences regarding the parameter estimation of these

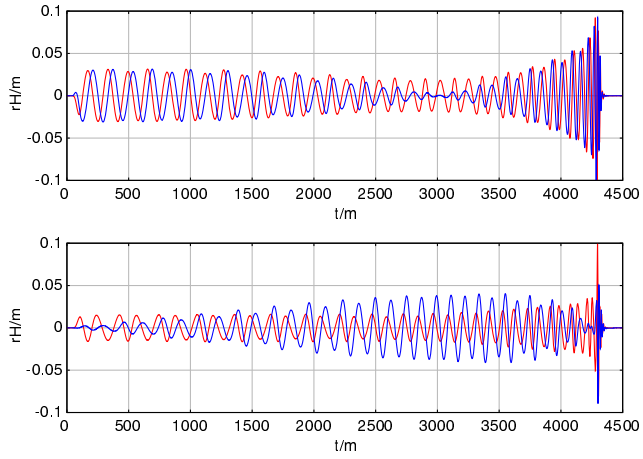

FIG. 3. The two polarizations of the waveform strain of the system with mass ratio $q = 1/7$ as seen from the z axis (the initial direction of the orbital angular momentum) (above) and the same waveform strain as seen from the y axis (below) reconstructed using modes up to $l_{\rm max} = 5$.

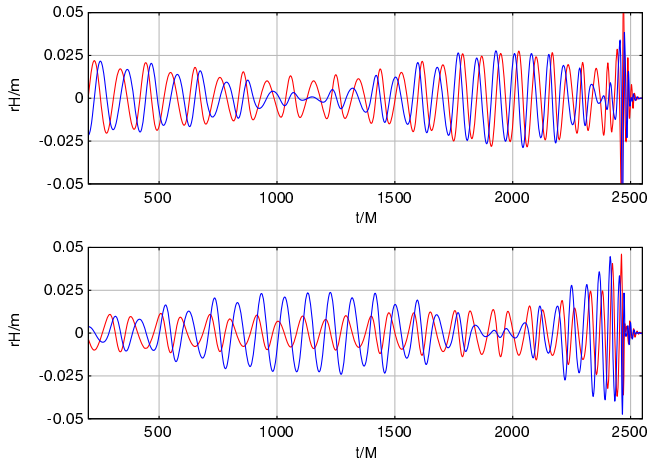

FIG. 4. The two polarizations of the waveform strain of the system with mass ratio $q = 1/15$ as seen from the z axis (the initial direction of the orbital angular momentum) (above) and the same waveform strain as seen from the y axis (below) reconstructed using modes up to $l_{\max} = 5$.

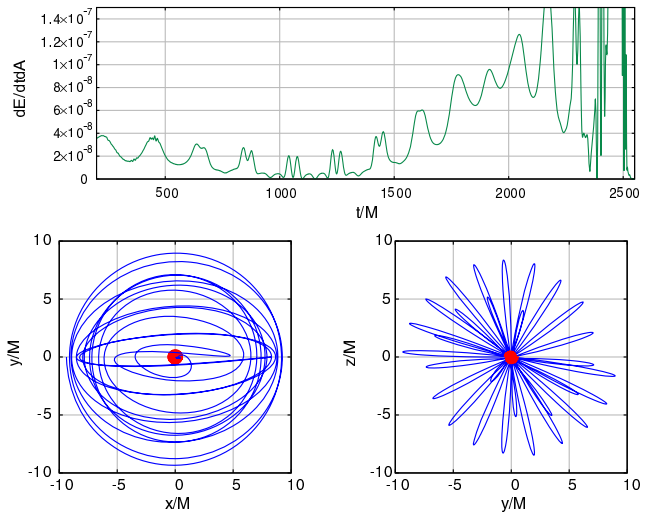

FIG. 5. The beaconing effect displayed by the power radiated for the binary case with mass ratio $q = 1/15$ as seen from the z axis (the initial direction of the orbital angular momentum) (above) and (below) the detail of the black hole trajectories in the initial orbital plane (left) and seen from an observer along the x axis (right).

systems via measurements of the (two polarizations of the) gravitational waves (see below).

Additionally, the effect is strongly dependent on which polarization of the gravitational waves we are observing. Figures 3 and 4 show that, while the amplitude of one of the polarizations remains slowly varying, the other has dramatic variations (like a breathing mode) on the scale of this $\vec{L}$-precessional period. The black hole trajectories also display a very rich pattern of polar precession until very late in the inspiral motion (bottom panels in Fig. 5.)

We provide in Table II the remnant properties of the final black of the two simulations. The modeling of the final mass, spin, and recoil of the final merged black hole has been the subject of many studies (see Ref. [5] and references therein). Also provided are the peak luminosity, amplitude, and frequency, that can be used for extending the modeling of those quantities [30,45] to precessing binaries with application to observations of gravitational waves from black hole binaries. Precessing binaries, as studied here, have very rich dynamics that makes it difficult to accurately model [40,46]. Here we provide two useful new data points for forthcoming modeling and testing.

To provide a measure of the accuracy of the simulations, we track the individual horizons of the large and small black holes, compute its masses and spins, and display them in Fig. 6. Those measurements are seen to be preserved at least to one part in 10^4 in the cases of the masses and one part in 10^3 in the cases of the spins. Absorption of gravitational waves plays an important role only early in the numerical evolution due to the initial data radiation content, and we hence use as the reference measure a settling time of $t_r = 200M$. The merger of the two holes creates a larger final hole with the mass and spin measured from its horizon as reported in Table II.

A. Comparisons with post-Newtonian waveforms and nonprecessing simulations

We looked at several cases comparing the numerical relativity (NR) waveforms to the corresponding PN approximated waveform. For nonprecessing configurations, to calculate the amplitude of the 22 mode of the strain, we use 3.5 PN orbital terms [47,48], and 1.5 PN precessing spin terms [49]. This calculation works for small inclination angles as well, but our beaconing cases in no way satisfy this approximation. This is evident when looking at the generated waveform. While it does show a beaconing effect, the amplitude is both qualitatively and quantitatively

TABLE II. Remnant properties of the beaconing simulations: final mass M_f/M and spin α_f, peak radiation $\mathcal{L}^{\rm peak}$ and frequency $M\Omega_{22}^{\rm peak}$, and recoil velocity $V_{\rm recoil}$. The final mass and spin are measured from the apparent horizon, and the recoil velocity, peak luminosity, frequency, and amplitude are calculated from the gravitational waveforms. Also given is the deviation of the angle between the initial total angular momentum and final spin, $\Delta\theta$.

Case	$q = 1/7$	$q = 1/15$
M_f/M	0.989 542	0.994 071
$\lvert\alpha_f\rvert$	0.466 308	0.716 323
$(\alpha_f^x, \alpha_f^y, \alpha_f^z)$	(−0.4621, −0.0358, 0.0510)	(−0.7162, 0.0045, −0.0102)
$\Delta\theta$	6.19°	1.27°
$V_{\rm recoil}$ [km/s]	275.2	78.1
$\mathcal{L}^{\rm peak}$	1.4598×10^{-4}	5.4498×10^{-5}
$M\Omega_{22}^{\rm peak}$	−0.2975	0.2184
$(\frac{r}{M})H_{22}^{\rm peak}$	0.1688	0.0764

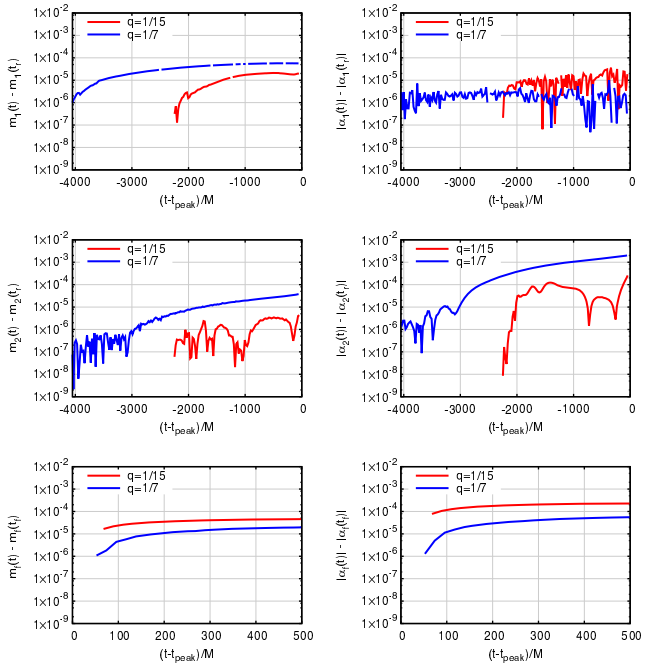

FIG. 6. The evolution of the horizon masses (left) and spins (right) for the individual black holes (labeled as 1 and 2) and the final merged hole (labeled as 3) for both cases with mass ratios $q = 1/7$ and $q = 1/15$. All differences (for horizons 1 and 2) are compared to the values at settling time $t_r = t_0 + 200M$ and to $50M$ after the peak of the gravitational wave radiation $t_f = t_{\rm peak} + 50M$ for horizon 3, where t_0 is the start of the simulation. Since we are comparing both $q = 1/7$ and $q = 1/15$ runs in the same plot and they have different run times, we shift the time of peak amplitude, $t_{\rm peak}$, to 0 for a better display.

different, with both polarizations losing power during the beaconing (compared to the NR case where this is exhibited only in the imaginary part). For comparisons with the beaconing cases, we use the 1.5 PN strain amplitude for generic inclination angles given in Appendix B of Ref. [49]. For the phasing information, in both cases we use a 3.5PN orbital evolution code with leading-order spin-spin terms and next-to-leading-order spin-orbit terms [50,51]. We can also use the NR trajectory information [52] for an even tighter hybrid comparison.

To add a further level of comparison, we produced two new sets of full numerical simulations with the same mass ratios $q = 1/7$ and $q = 1/15$ but for nonprecessing and nonspinning binaries. To calculate the match between NR and PN waveforms, we use a complex match [53] which factors in both polarizations of the waveforms, a starting frequency of 30 Hz, and the "ZERO_DET_high_P" analytic noise curve for advanced LIGO [54]. We choose the mass of the systems such that the waveforms start at 30 Hz in the LIGO band. The results of the matches between the 22 mode of the strain for the NR waveform and the PN waveform are given in Table III for the six different cases (nonprecessing, nonspinning and beaconing for $q = 7$ and $q = 15$). We show the results for both PN waveforms where the phasing information in the amplitude is supplied by PN or by NR. Since the complex match allows for maximization over time and phase shift, we find an exceptionally good result when using the NR phase information.

TABLE III. Matches between PN and NR waveforms using the PN phase ($\phi_{\rm PN}$) or the NR phase ($\phi_{\rm NR}$) for the PN waveform and the minimal SNR needed to distinguish between the two waveforms, given the mismatch ($\mathrm{SNR}^2 \geq \frac{1}{1-\mathcal{M}}$.).

Case	$\mathcal{M}$ $\phi_{\rm PN}$	SNR $\phi_{\rm PN}$	$\mathcal{M}$ $\phi_{\rm NR}$	SNR $\phi_{\rm NR}$
NS7	0.917	3.5	0.998	22.4
NS15	0.693	1.8	0.994	12.9
AS7	0.903	3.2	0.999	31.6
AS15	0.802	2.3	0.994	12.9
GWB7	0.837	2.5	0.997	18.3
GWB15	0.807	2.3	0.991	10.5

Figure 7 shows the NR waveforms for the 22 modes of the strain for the nonprecessing and beaconing $q = 1/7$ simulations. The waveforms are aligned at the same initial frequency, and the phase is shifted to agree at the start of the waveform. Similarly, we show the waveforms for the $q = 1/15$ case in Fig. 8. Note in the latter, for the imaginary component of the polarization, the clear change from the "in phase" before the half beaconing period to the exactly 180° "out of phase" right after, until the beaconing period is completed. This shows the expected change from face on to face off of the beaconing binary compared to its nonprecessing counterpart.

To determine if the nonprecessing waveforms are comparable to the beaconing waveforms along different lines of sight, we ran a series of 390 625 matches over the sky

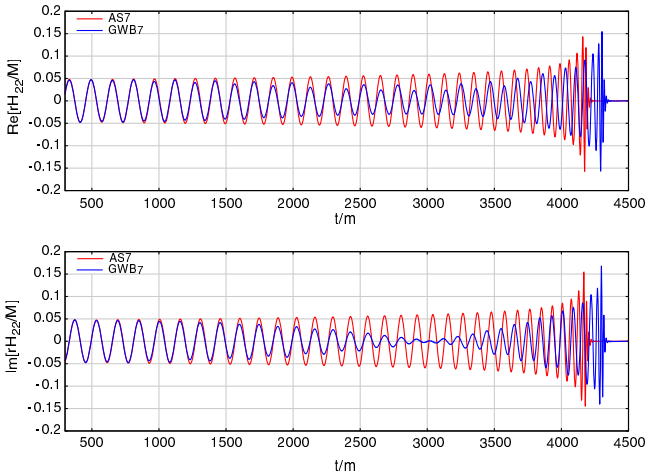

FIG. 7. The real and imaginary parts of the 22 mode of the beaconing and nonprecessing $q = 1/7$ case. In blue (red) is the 22 mode strain waveform of the beaconing (nonprecessing) waveform. The top panel is the real part, and the bottom panel is the imaginary part. Both are extrapolated to an infinite observer location.

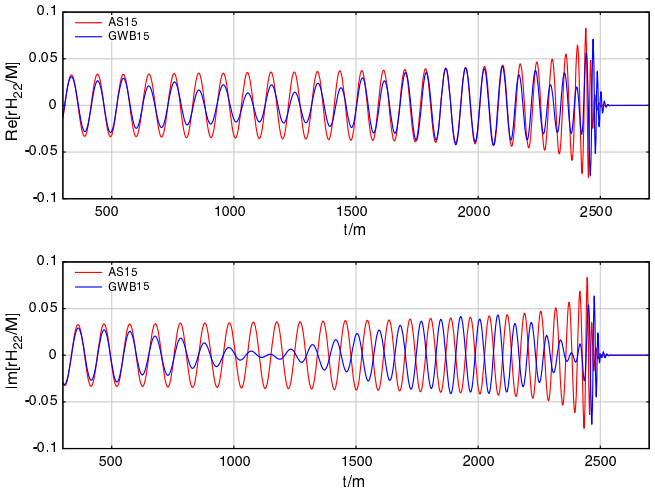

FIG. 8. The real and imaginary parts of the 22 mode of the beaconing and nonprecessing $q = 1/15$ case. In blue (red) is the 22 mode strain waveform of the beaconing (nonprecessing) waveform. The top panel is the real part, and the bottom panel is the imaginary part. Both are extrapolated to an infinite observer location.

angles of both waveforms. That is, we reconstructed $\frac{r}{M}h_{\rm AS}(\theta_{\rm AS},\phi_{\rm AS})$ and $\frac{r}{M}h_{\rm GWB}(\theta_{\rm GWB},\phi_{\rm GWB})$ using modes up to $\ell = 6$ and varied over $\theta_{\rm AS},\phi_{\rm AS},\theta_{\rm GWB},\phi_{\rm GWB}$ calculating the match between the nonprecessing and beaconing waveforms. We keep the masses constant such that the starting frequency of the waveform is 30 Hz. For the $q = 1/7$ case, we find the best match of 0.445, and for $q = 1/15$, we find 0.788. This displays the relevance of the black hole spins in the late dynamics of the binary at the level of gravitational waveforms.

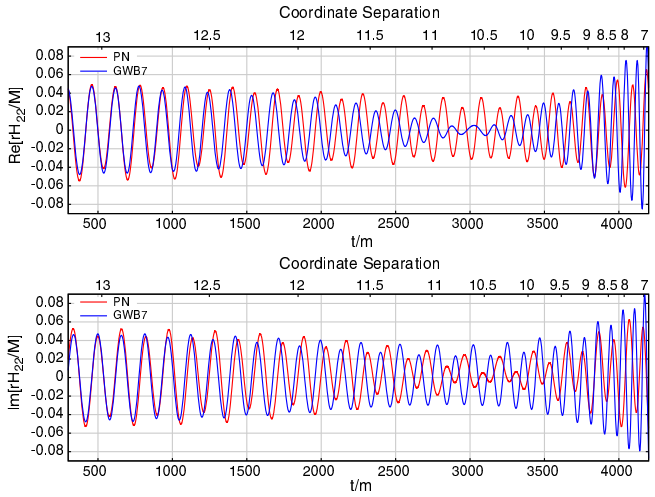

FIG. 9. The real and imaginary parts of the 22 mode of the beaconing $q = 1/7$ case. In blue is the 1.5 PN 22 mode strain waveform, and in red is the NR 22 mode strain waveform extrapolated to an infinite observer location. The top x axis gives the NR coordinate separation of the waveform, and the bottom x axis gives the time.

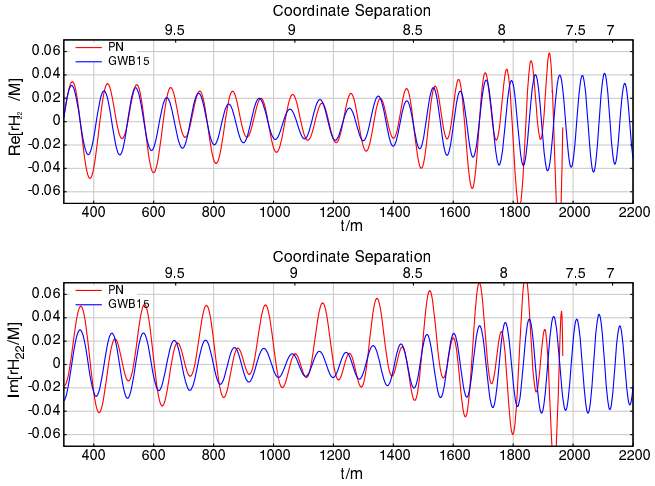

FIG. 10. The real and imaginary parts of the 22 mode of the beaconing $q = 1/15$ case. In blue is the 1.5 PN 22 mode strain waveform, and in red is the NR 22 mode strain waveform extrapolated to an infinite observer location. The top x axis gives the NR coordinate separation of the waveform, and the bottom x axis gives the time.

Figures 9 and 10 show the 22 mode NR and PN strain waveforms for the $q = 1/7$ and $q = 1/15$ beaconing cases. The mismatch among them is apparent and displays the relevance of using accurate NR waveforms for the binary's parameter estimation.

IV. CONCLUSIONS AND DISCUSSION

We have studied binary black hole configurations that at the time of the late inspiral are caught in the middle of a transitional precession. This is a relatively common phase for small mass ratio ($q < 1/4$) *retrograde* merging binaries to go through. As shown by our simulations, schematically depicted in Fig. 1, the spin of the large hole $\vec{S}$ does not have to be particularly fine-tuned to almost exactly oppose to the orbital angular momentum. The strong dynamics of the merger notably decreases the magnitude of $\vec{L}$, eventually matching the spin component along it (while also accelerating the precession frequency), leading to the formation of the final remnant black hole before the system completes the transitional precession (falling into a spin-dominated simple precessional state, as predicted in Ref. [11]). On the contrary, we find that $\vec{S}$ and $\vec{L}$ still roughly precess around a mostly unchanged (in direction) total angular momentum $\hat{J}$, displaying a total L flip.

These orbital dynamics have the consequence of generating particular patterns of gravitational radiation: strong oscillations in the amplitude of the waveforms and distinct behavior in each polarization. These special features can be important to identify binary parameters in this stage when observing gravitational waves. It can also break current model pseudodegeneracies in the determination of the

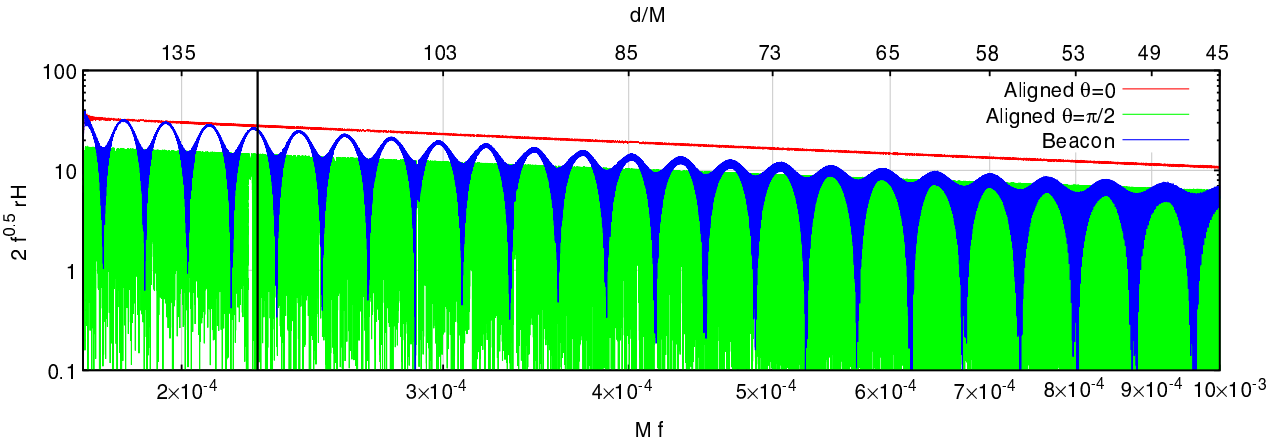

FIG. 11. The spectral density of the 22 mode of the beaconing $q = 1/15$ case (evolved with PN from $r = 150M$) compared to the nonprecessing case as seen face on and face off. In blue is the strain waveform of the beaconing binary, and in red (green) is the strain waveform of an equivalent spinning but nonprecessing binary as seen from face on (face off). The top axis gives the separation, r/M, of the nonprecessing binary, and the bottom axis gives the waveform frequency Mf. The black vertical line represents the beaconing frequency before the merger.

binary's orientation and individual black holes' spins. This highlights the importance of observing the two gravitational wave polarizations (with current detectors networks and in new third-generation designs) and, potentially, could allow tracking the observation of these systems in a multigravitational frequency band [55–57].

At the low beaconing frequencies, the spectrum of radiation can be estimated via a PN evolution from an initial separation of $r = 150M$ and compared to a nonprecessing binary with the same initial projected spin along the orbital angular momentum. Figure 11 displays such spectra and shows that the beaconing amplitude oscillates between the face-on and face-off aligned cases of the nonprecessing binary. This shows that the beaconing effect gives observers of gravitational waves a much higher chance of seeing the binary at its peak amplitude. The strong oscillations in amplitude shown in Figs. 3 and 4, comparable to the orbital amplitude oscillations, could lead to the possibility of also detecting systems at lower frequencies, the *beaconing* frequencies. Let us consider a simple modeling of one of the polarizations of the waveform as $H(t) = A(t)\cos(\Omega_L t)\sin(2\Omega_{\rm orb} t)$, where the amplitude $A(t)$ varies at the larger inspiral rate and Ω_L corresponds to the "beaconing" frequency scale and provides the envelope of the higher gravitational wave frequency, that for the leading (2,2) modes is twice the orbital frequency, $\Omega_L(r_c)$. Using basic trigonometric identities for the addition of angles, we obtain $H(t) = A(t)\{\sin([2\Omega_{\rm orb} + \Omega_L]t) + \sin([2\Omega_{\rm orb} - \Omega_L]t)\}/2$. Since, in general, $\Omega_L \ll 2\Omega_{\rm orb}$, we have that both components lie close to $2\Omega_{\rm orb}$ and, hence, in the higher frequency band. This is, of course, a single-frequency and single-mode analysis and the spectrum of gravitational radiation is rather continuous due to the merger process and multimode, but this simple model displays that it is difficult to generate much lower frequency gravitational waves with significant amplitude. How to detect the beaconing effect at low frequencies lies outside the scope of this paper, but it is an interesting challenge for multiband data analysis.

The results reported in this paper highlight the fact that there is still important information to extract from observations of gravitational waves. The relevance of using accurate templates from numerical simulations was already found for GW170104 in Ref. [35], where a more robust case for precession is made by directly using numerical relativity waveforms (see Fig. 8 there). Not only is the accuracy of the orbital and spin dynamics important here, but also the inclusion of several (nonleading) modes (up to $\ell = 5$) to account for effects of the flip of the orbital angular momentum during the period of observations. Note that the phenomenological models, like SEOBNRv3, currently used by LIGO [58] have not been validated in this range of mass ratios, and, as shown in Refs. [35,59,60], they differ substantially from NR simulations (e.g., mismatch $\gg 1/\mathrm{SNR}^2 \sim 10^{-3}$, the maximum allowed to have any chance of consistent parameter inference). Particularly the *ad hoc* approach to a precessing merger (not equivalent to the rotation of a nonprecessing system, as used by the PhenomP model [61]) may lead to misevaluations of, for instance, recoil velocities, here reported in Table II.

Finally, let us mention that, for the last beaconing period to be completely in the LIGO band, the total mass of the binaries has to be in a range of masses. Successive improvements in sensitivity will lead to observations of smaller mass ratio binaries. For instance, for the $q = 1/15$ binary to start in the band (above 20 Hz), the total mass of the system has to be lower than 91 $M_\odot$, and for the ringdown of the merged black hole to be in the band (below 1000 Hz), the total mass has to be higher than 16 $M_\odot$. A similar analysis can be done for major mergers sources

for LISA operating in the millihertz band and the pulsar timing arrays operating in the nanohertz band by scaling up the total mass of the binaries to millions and billions of solar masses.

ACKNOWLEDGMENTS

The authors thank M. Campanelli, R. O'Shaughnessy, and Y. Zlochower for discussions on this work. The authors gratefully acknowledge the National Science Foundation (NSF) for financial support from Grants No. PHY-1607520, No. PHY-1707946, No. ACI-1550436, No. AST-1516150, No. ACI-1516125, and No. PHY-1726215. This work used the Extreme Science and Engineering Discovery Environment (XSEDE) [allocation TG-PHY060027N], which is supported by NSF Grant No. ACI-1548562. Computational resources were also provided by the NewHorizons, BlueSky Clusters, and Green Prairies at the Rochester Institute of Technology, which were supported by NSF Grants No. PHY-0722703, No. DMS-0820923, No. AST-1028087, No. PHY-1229173, and No. PHY-1726215.

APPENDIX: MERGER PROPERTIES OF THE NONPRECESSING AND NONSPINNING SIMULATIONS

For the sake of completeness and future reference, we provide the remnant properties of the nonspinning and nonprecessing simulations in Table IV.

TABLE IV. Remnant properties: final mass M_f/M and spin α_f, peak radiation $\mathcal{L}^{\rm peak}$ and frequency $M\Omega_{22}^{\rm peak}$, and recoil velocity $V_{\rm recoil}$. The final mass and spin are measured from the apparent horizon, and the recoil velocity, peak luminosity, frequency, and amplitude are calculated from the gravitational waveforms. After each column is the percent difference between the measured value and the analytic fit [5].

Case	NS7	%Diff.	NS15	%Diff.	AS7	%Diff.	AS15	%Diff.
M_f/M	0.9878	0.016%	0.9948	0.011%	0.9909	0.004%	0.9956	0.005%
α_f^z	0.3364	0.067%	0.1884	1.810%	−0.0791	0.058%	−0.0283	1.595%
$V_{\rm recoil}$ [km/s]	95	0.744%	33	0.085%	131	2.753%	38	1.109%
$\mathcal{L}^{\rm peak}$	$1.611e-4$	0.312%	$4.611e-5$	0.529%	$1.205e-5$	4.525%	$3.911e-5$	2.541%
$M\Omega_{22}^{\rm peak}$	0.3045	0.082%	0.2902	0.475%	0.2631	0.377%	0.2665	2.168%
$(\frac{r}{M})H_{22}^{\rm peak}$	0.1611	0.404%	0.0853	0.642%	0.1578	0.032%	0.0836	0.471%

[1] F. Pretorius, Phys. Rev. Lett. **95**, 121101 (2005).
[2] M. Campanelli, C. O. Lousto, P. Marronetti, and Y. Zlochower, Phys. Rev. Lett. **96**, 111101 (2006).
[3] J. G. Baker, J. Centrella, D.-I. Choi, M. Koppitz, and J. van Meter, Phys. Rev. Lett. **96**, 111102 (2006).
[4] M. Campanelli, C. O. Lousto, and Y. Zlochower, Phys. Rev. D **74**, 041501(R) (2006).
[5] J. Healy and C. O. Lousto, Phys. Rev. D **97**, 084002 (2018).
[6] M. Campanelli, C. O. Lousto, Y. Zlochower, and D. Merritt, Astrophys. J. **659**, L5 (2007).
[7] C. O. Lousto and Y. Zlochower, Phys. Rev. Lett. **107**, 231102 (2011).
[8] C. O. Lousto, J. Healy, and H. Nakano, Phys. Rev. D **93**, 044031 (2016).
[9] M. Kesden, D. Gerosa, R. O'Shaughnessy, E. Berti, and U. Sperhake, Phys. Rev. Lett. **114**, 081103 (2015).
[10] C. O. Lousto and J. Healy, Phys. Rev. D **93**, 124074 (2016).
[11] T. A. Apostolatos, C. Cutler, G. J. Sussman, and K. S. Thorne, Phys. Rev. D **49**, 6274 (1994).
[12] W. Del Pozzo, A. Sesana, and A. Klein, Mon. Not. R. Astron. Soc. **475**, 3485 (2018).
[13] R. Tso, D. Gerosa, and Y. Chen, arXiv:1807.00075.
[14] Y. Zlochower, J. G. Baker, M. Campanelli, and C. O. Lousto, Phys. Rev. D **72**, 024021 (2005).
[15] P. Marronetti, W. Tichy, B. Brügmann, J. Gonzalez, and U. Sperhake, Phys. Rev. D **77**, 064010 (2008).
[16] C. O. Lousto and Y. Zlochower, Phys. Rev. D **77**, 024034 (2008).
[17] F. Löffler, J. Faber, E. Bentivegna, T. Bode, P. Diener, R. Haas, I. Hinder, B. C. Mundim, C. D. Ott, E. Schnetter, G. Allen, M. Campanelli, and P. Laguna, Classical Quantum Gravity **29**, 115001 (2012).
[18] Einstein Toolkit, http://einsteintoolkit.org.
[19] Cactus Computational Toolkit, http://cactuscode.org.
[20] E. Schnetter, S. H. Hawley, and I. Hawke, Classical Quantum Gravity **21**, 1465 (2004).
[21] J. Thornburg, Classical Quantum Gravity **21**, 743 (2004).
[22] O. Dreyer, B. Krishnan, D. Shoemaker, and E. Schnetter, Phys. Rev. D **67**, 024018 (2003).
[23] M. Campanelli, C. O. Lousto, Y. Zlochower, B. Krishnan, and D. Merritt, Phys. Rev. D **75**, 064030 (2007).
[24] M. Campanelli and C. O. Lousto, Phys. Rev. D **59**, 124022 (1999).

[25] C. O. Lousto and Y. Zlochower, Phys. Rev. D **76**, 041502(R) (2007).
[26] H. Nakano, J. Healy, C. O. Lousto, and Y. Zlochower, Phys. Rev. D **91**, 104022 (2015).
[27] J. Healy, C. O. Lousto, H. Nakano, and Y. Zlochower, Classical Quantum Gravity **34**, 145011 (2017).
[28] C. O. Lousto and Y. Zlochower, Phys. Rev. Lett. **106**, 041101 (2011).
[29] J. Healy, C. O. Lousto, and Y. Zlochower, Phys. Rev. D **90**, 104004 (2014).
[30] J. Healy and C. O. Lousto, Phys. Rev. D **95**, 024037 (2017).
[31] J. Healy, C. O. Lousto, and Y. Zlochower, Phys. Rev. D **96**, 024031 (2017).
[32] Y. Zlochower, J. Healy, C. O. Lousto, and I. Ruchlin, Phys. Rev. D **96**, 044002 (2017).
[33] J. Healy, C. O. Lousto, I. Ruchlin, and Y. Zlochower, Phys. Rev. D **97**, 104026 (2018).
[34] G. Lovelace *et al.*, Classical Quantum Gravity **33**, 244002 (2016).
[35] J. Healy *et al.*, Phys. Rev. D **97**, 064027 (2018).
[36] J. Healy, C. O. Lousto, Y. Zlochower, and M. Campanelli, Classical Quantum Gravity **34**, 224001 (2017).
[37] J. Healy, C. O. Lousto, J. Lange, R. O'Shaughnessy, Y. Zlochower, and M. Campanelli, arXiv:1901.02553.
[38] https://ccrg.rit.edu/ RITCatalog/.
[39] C. O. Lousto and Y. Zlochower, Phys. Rev. D **89**, 021501 (2014).
[40] C. O. Lousto and Y. Zlochower, Phys. Rev. D **89**, 104052 (2014).
[41] C. O. Lousto and Y. Zlochower, Phys. Rev. D **88**, 024001 (2013).
[42] E. Racine, Phys. Rev. D **78**, 044021 (2008).
[43] C. O. Lousto, H. Nakano, Y. Zlochower, and M. Campanelli, Phys. Rev. D **81**, 084023 (2010).
[44] E. Racine, A. Buonanno, and L. E. Kidder, Phys. Rev. D **80**, 044010 (2009).
[45] X. Jiménez-Forteza, D. Keitel, S. Husa, M. Hannam, S. Khan, and M. Pürrer, Phys. Rev. D **95**, 064024 (2017).
[46] Y. Zlochower and C. O. Lousto, Phys. Rev. D **92**, 024022 (2015).
[47] L. Blanchet, G. Faye, B. R. Iyer, and S. Sinha, Classical Quantum Gravity **25**, 165003 (2008).
[48] G. Faye, S. Marsat, L. Blanchet, and B. R. Iyer, Classical Quantum Gravity **29**, 175004 (2012).
[49] K. G. Arun, A. Buonanno, G. Faye, and E. Ochsner, Phys. Rev. D **79**, 104023 (2009).
[50] A. Buonanno, Y. Chen, and T. Damour, Phys. Rev. D **74**, 104005 (2006).
[51] T. Damour, P. Jaranowski, and G. Schafer, Phys. Rev. D **77**, 064032 (2008).
[52] M. Campanelli, C. O. Lousto, H. Nakano, and Y. Zlochower, Phys. Rev. D **79**, 084010 (2009).
[53] H.-S. Cho, E. Ochsner, R. O'Shaughnessy, C. Kim, and C.-H. Lee, Phys. Rev. D **87**, 024004 (2013).
[54] https://dcc.ligo.org/LIGO-T0900288/public.
[55] A. Sesana, Phys. Rev. Lett. **116**, 231102 (2016).
[56] S. Vitale, Phys. Rev. Lett. **117**, 051102 (2016).
[57] K. W. K. Wong, E. D. Kovetz, C. Cutler, and E. Berti, Phys. Rev. Lett. **121**, 251102 (2018).
[58] S. Babak, A. Taracchini, and A. Buonanno, Phys. Rev. D **95**, 024010 (2017).
[59] A. R. Williamson, J. Lange, R. O'Shaughnessy, J. A. Clark, P. Kumar, J. Caldern Bustillo, and J. Veitch, Phys. Rev. D **96**, 124041 (2017).
[60] J. Blackman, S. E. Field, M. A. Scheel, C. R. Galley, C. D. Ott, M. Boyle, L. E. Kidder, H. P. Pfeiffer, and B. Szilgyi, Phys. Rev. D **96**, 024058 (2017).
[61] M. Hannam, P. Schmidt, A. Bohé, L. Haegel, S. Husa, F. Ohme, G. Pratten, and M. Pürrer, Phys. Rev. Lett. **113**, 151101 (2014).